Design of a Multi-Arm Surgical Robotic System for Dexterous Manipulation

Zhi Li
Electrical and Computer Engineering,
Duke University,
Durham, NC 27708
e-mail: zhi.li2@duke.edu

Dejan Milutinović
Computer Engineering,
University of California, Santa Cruz,
Santa Cruz, CA 95064
e-mail: Dejan@soe.ucsc.edu

Jacob Rosen
Bionics Lab,
Mechanical and Aerospace Engineering,
University of California, Los Angeles,
Los Angeles, CA 90095
e-mail: rosen@seas.ucla.edu

Surgical procedures are traditionally performed by two or more surgeons along with staff nurses: one serves as the primary surgeon and the other as his/her assistant. Introducing surgical robots into the operating room has significantly changed the dynamics of interaction between the surgeons and with the surgical site. In this paper, we design a surgical robotic system to support the collaborative operation of multiple surgeons. This Raven IV surgical robotic system has two pairs of articulated robotic arms with a spherical configuration, each arm holding an articulated surgical tool. It allows two surgeons to teleoperate the Raven IV system collaboratively from two remote sites. To optimize the mechanism design of the Raven IV system, we configure the link architecture of each robotic arm, along with the position and orientation of the four bases and the port placement with respect to the patient's body. The optimization considers seven different parameters, which results in 2.3×10^{10} system configurations. We optimize the common workspace and the manipulation dexterity of each robotic arm. We study here the effect of each individual parameter and conduct a brute force search to find the optimal set of parameters. The parameters for the optimized configuration result in an almost circular common workspace with a radius of 150 mm, accessible to all four arms.
[DOI: 10.1115/1.4034143]

1 Introduction

Surgical robots recently introduced into the operating room have significantly changed the way surgery is conducted. Together with the clinical breakthroughs in new surgical techniques, these technological innovations in robotic system development have improved the quality and outcomes of surgery. In the last decade, research efforts have been dedicated to developing surgical robotic systems that show high levels of manipulation dexterity and precision not achievable by the surgeons' hand, provide viewing angles otherwise unavailable to surgeons' views, and minimize the trauma to the tissue surrounding the surgical site. Advancements in surgical robot technology have led to the development of new surgical techniques that would otherwise be impossible.

Surgical procedures are traditionally performed by two or more surgeons, along with staff nurses. Due to the heavy cognitive load and manual demands of surgical procedures, the collaborative effort of two or more surgeons is often required. With the introduction of surgical robots into operating rooms, the dynamics between the primary and assisting surgeons changes significantly. The primary surgeon, who controls the surgical robot, is immersed in a surgical console and is physically removed from the surgical site itself, while the assistant is usually located next to the patient and holds another set of nonrobotic surgical tools. Reproducing the interaction of two surgeons with the surgical site using surgical robotic systems requires at least four robotics arms and two stereo cameras rendering the surgical site. Once multiple robotic arms are introduced, several operational modes are available in which each pair of arms can be under full human control or in a semi-autonomous mode (supervisory control).

In spite of the advantages, the introduction of multiple robotic arms into a relatively small space presents challenges. From the operational perspective, there is a need to maximize the common workspace that is accessible by the end effectors of all four arms. This common workspace needs to overlap with the surgical site dictated by the patient's internal anatomy. Increasing the common workspace may lead to larger robotic arms, which in turn may result in patient–robot or robot–robot collisions.

Previous research efforts mainly focused on the design of port placement for cardiac procedures while using several existing robotic arm architectures, such as the Zeus [1,2] or DaVinci [3,4] or a similar, four-bar mechanism [5] inserted between the ribs. With the introduction of four robotic arms, a new optimization approach is required for designing the size and shape of the common workspace of the four robotic arms while ensuring the kinematic performance of each robotic arm. The scope of this research effort is a kinematic optimization of the surgical robotic arms in terms of their structural configurations, as well as their positions (port placement) and orientations with respect to the patient.

In this research, we introduce the mechanism design and optimization of the Raven IV (Fig. 1) surgical robotic system. It has two pairs of articulated robotic arms and, therefore, supports two

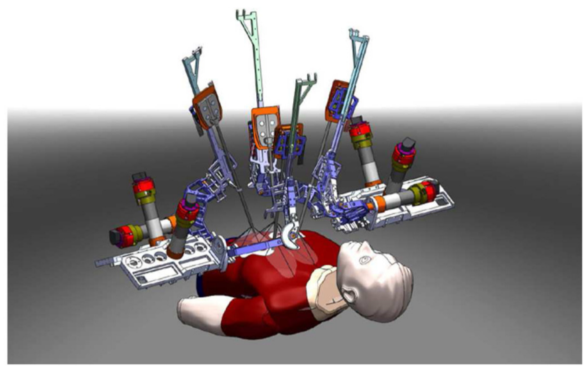

Fig. 1 Raven IV Surgical Robot System—CAD rendering of the four Raven's arms interacting with the patient. In the figure, most of the actuators were removed from the base of each arm to expose to the rest of the arms and the shared workspace. The workspaces are marked with transparent cones and their intersection defines the shared workspace.

Manuscript received October 7, 2015; final manuscript received June 20, 2016; published online October 11, 2016. Assoc. Editor: Satyandra K. Gupta.

surgeons in collaboration using two surgical consoles that are located either next to the patient or at two remote locations. Raven IV is the second generation of Raven I [6–16]. The kinematic optimization of Raven I was based on the analysis of the workspace of a single arm [15,17]. Several major structural changes are made to minimize the footprint of the individual robotic arm including the following: (1) all the actuators located on the base of the robot are mounted on top of the base allowing the base to be moved closer to the patient body; (2) the dimensions of the actuation package are reduced; (3) the link lengths are changed based on reported results; (4) the tensioning mechanisms of the cables are relocated in the base plate to provide better access and solid performance; (5) a universal tool interface is designed to accept surgical robotics tools from different vendors; and (6) a unique tool with a dual joint wrist is designed and incorporated into the system.

In addition, we propose a method to optimize the geometry of the four robotic arms and the relative position and orientation of their bases. The cost function in our optimization accounts for (1) the size and shape of the common workspace of all the arms, (2) the mechanism isotropy, and (3) the mechanism stiffness. In minimally invasive surgery, the surgical tools designed to be attached to a surgical robotic arm are the same as the ones used in traditional surgery. The optimization does not target a specific internal organ or anatomical structure, but is instead based on sizes of patient and animal models. Our method is proposed for the optimization of the Raven IV surgical robotic system, but can be generally applied to the optimization of a wider spectrum of similar robotic systems.

2 Methodology

We propose a method to optimize the kinematics of the Raven IV surgical robotic arms. In this section, we present the forward and inverse kinematics, the Jacobian matrix, and the cost function for the optimization. The cost function accounts for the link lengths of the spherical mechanism, the port spacing, the base orientations of the robotic arms, and the manipulation isotropy in the common workspace.

The Raven IV surgical robot system consists of two pairs of surgical robotic arms. These two pairs are mirror images of each other, which result in their symmetric kinematics. Each surgical robot arm has seven degrees-of-freedom (DOFs): six DOFs for positioning and orienting the end effector and one for opening and closing the surgical tool attached to the surgical arm.

The base frame is located at the converging center of the spherical mechanism, which is formed by the first three links of a Raven IV arm (Fig. 2(*a*)). The Denavit-Hartenberg (DH) Parameters (see

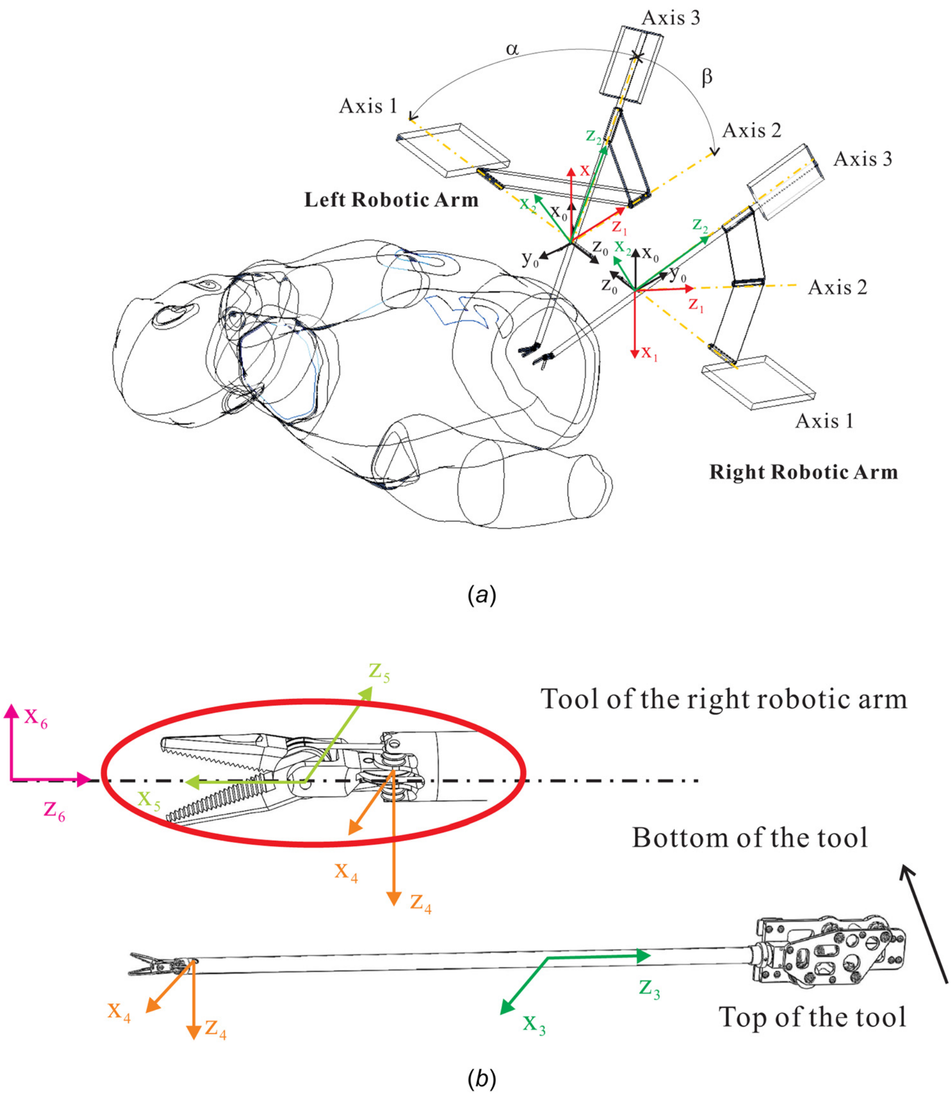

Fig. 2 Reference frame of the Raven IV surgical robotic system: (*a*) surgical robot arm and (*b*) surgical tool

Table 1 DH Parameters for Raven IV arms

Robot	$i-1$	i	α_i	a_i	d_i	θ_i
Left	0	1	$\pi-\alpha$	0	0	$\theta_1(t)$
Robot	1	2	$-\beta$	0	0	$-\theta_2(t)$
(1,3)	2	3	0	0	0	$\pi/2-\theta_3(t)$
	3	4	$-\pi/2$	0	$d_4(t)$	0
	4	5	$\pi/2$	A_5	0	$\pi/2-\theta_5$
	5	6	$-\pi/2$	0	0	$\pi/2+\theta_6$
Right	0	1	$\pi-\alpha$	0	0	$\pi-\theta_1(t)$
Robot	1	2	$-\beta$	0	0	$\theta_2(t)$
(2,4)	2	3	0	0	0	$\pi/2+\pi+\theta_3(t)$
	3	4	$-\pi/2$	0	$d_4(t)$	0
	4	5	$-\pi/2$	A_5	0	$\pi/2+\theta_5$
	5	6	$-\pi/2$	0	0	$\pi/2-\theta_6$
Range	$\theta_1 \in [0\,\text{deg}, 90\,\text{deg}]$			$\theta_2 \in [20\,\text{deg}, 140\,\text{deg}]$		
	$\theta_3 \in [-86\,\text{deg}, 86\,\text{deg}]$			$d_4 \in [0, 250]$ mm		
	$\theta_5 \in [-86\,\text{deg}, 86\,\text{deg}]$			$\theta_6 \in [-86\,\text{deg}, 86\,\text{deg}]$		

Table 1) are derived with the standard method defined by Ref. [18]. The derivation of the forward and inverse kinematics is presented in Appendix.

The design of the surgical tools follows the generic geometry of a minimally invasive surgical tool. Thus, our method focuses on optimizing the shape of common workspace and the manipulability in it, and will determine the geometry of the first two links and the relative positions of the bases of the four Raven arms with respect to each other.

2.1 The Common Workspace and the Reference Plane.

The common workspace of our surgical system is the intersection of the workspaces of all the four Raven arms. Figure 3 depicts the arrangement of the four Raven arms with respect to each other. The gray bars represent the bases of the arms, while the magenta and the cyan bars represent the first and the second links of each arm, respectively. The common workspace of the four Raven IV arms is three-dimensional (3D). When optimizing the mechanical design of the system, we define a reference 2D plane, which is 150 mm below the plane that includes the ports of the four surgical arms. Typically, the surgical tools are inserted half way into the patient when the tool tips are operating in the reference plane. Since the surgical tools frequently operate in the reference plane, we decide to optimize the geometry of the projection of the 3D common workspace on this plane, as well as the manipulability within the projected area. In the rest of the paper, we will refer this area as the *common workspace* for simplicity.

2.2 Area–Circumference Ratio.

We want to optimize the shape of the common workspace in addition to maximizing its size. The optimized common workspace should be a circular area as possible so that the surgical tools are given free space to move uniformly in any direction. Here we define a variable ς, which is the ratio between the area and its circumference, to collectively evaluate the area and shape of the common workspace (see Eq. (1))

$$\varsigma = \frac{\text{Area}}{\text{Circumference}} \tag{1}$$

According to the *isoperimetric inequality*, the circle has the largest possible area among all the shapes with the same circumference. The area–circumference ratio of a circle ς_c is proportional to its radius r

$$\varsigma = \frac{\pi r^2}{2\pi r} = \frac{r}{2} \tag{2}$$

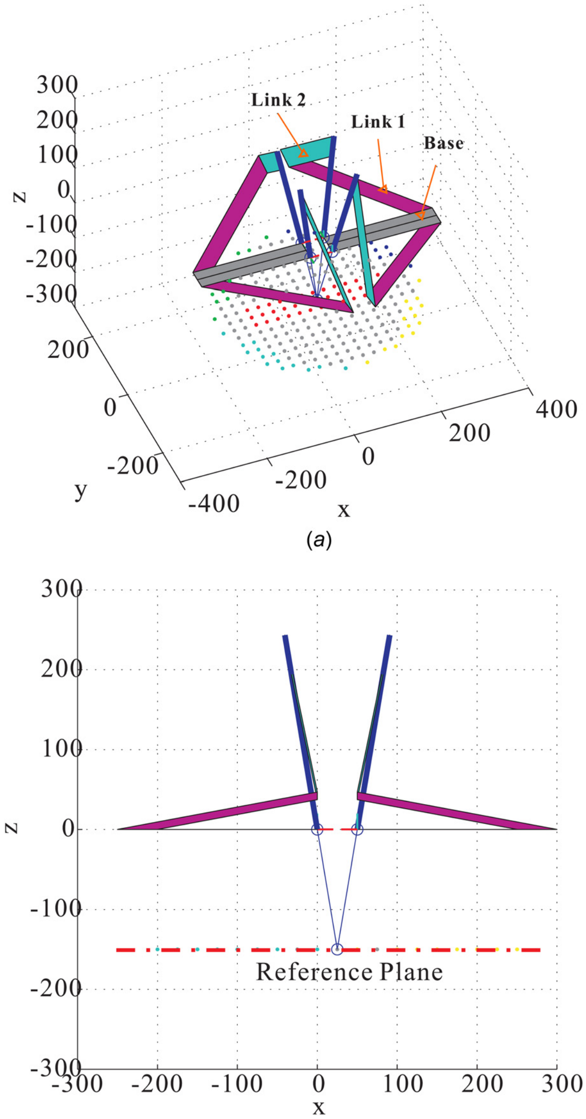

(*a*)

(*b*)

Fig. 3 The common workspace projected onto the reference plane: (*a*) 3D view and (*b*) projection onto the *x*–*z* plane. (unit: mm)

Practically, the common workspace has an amorphic shape that cannot be analytically expressed. However, maximizing ς will result in the common workspace that is as close to a circle as possible.

Figure 4 shows two common workspaces of two Raven arms, resulting from different link lengths. The common workspace depicted in Fig. 4(*b*) (with $\varsigma = 4.48$) has the preferred shape compared to the workspace illustrated in Fig. 4(*a*).

2.3 Mechanism Isotropy.

Isotropy measures the kinematic manipulability of the configuration of a mechanism. Its value ranges between 0 and 1. A mechanism is mechanically locked at the configuration where the isotropy is zero, losing one or more DOF. At a configuration where the isotropy is one, the mechanism is able to move equally in all directions and, therefore, has the best mapping between the joint space and the end effector space. The isotropy is computed as one over the condition number of the Jacobian matrix $\mathbf{J}$ (Eq. (3)).

$$\text{Iso} = \frac{1}{\text{Condition number of } \mathbf{J}} \tag{3}$$

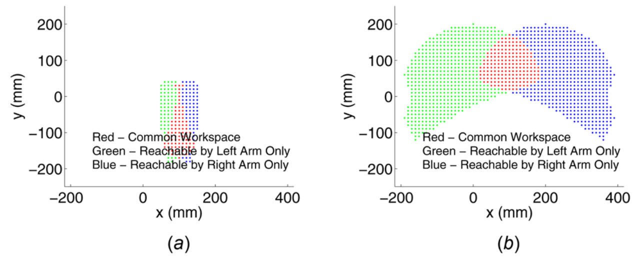

Fig. 4 Example of two typical common workspaces of two Raven arms constructed for two different link lengths defined by α and β: (*a*) two-arm configuration defined by the link lengths $\alpha = 65$ deg, and $\beta = 15$ deg resulting in $\varsigma = 2.23$ and (*b*) two-arm configuration defined by the link lengths $\alpha = 65$ deg, $\beta = 80$ deg resulting in $\varsigma = 4.48$

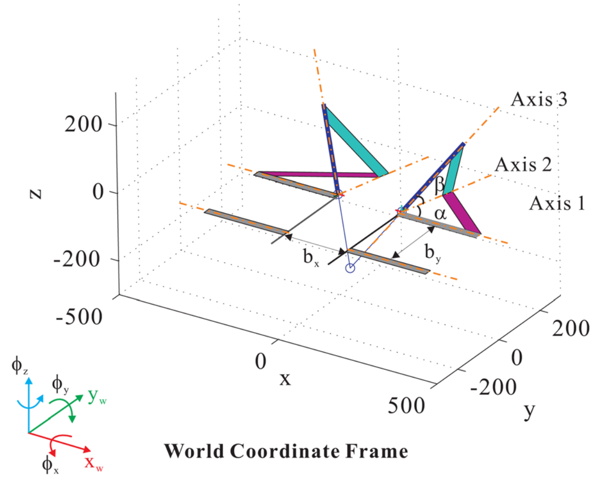

Fig. 5 Parameters for the optimization of the common workspace (unit: mm)

To evaluate the isotropy of a Raven IV arm, we analytically derive the Jacobian matrix using the velocity propagation method. The angular and the linear velocities are propagated iteratively from frame $\imath$ to frame $\imath + 1$ as:

$$^{i+1}\omega_{i+1} = ^{ii+1}R^{i}\omega_i + \dot{\theta}_{i+2}\hat{Z}_{i+1} \tag{4}$$

$$^{i+1}\mathbf{v}_{i+1} = ^{ii+1}R(^{i}\omega_i \times ^{i}P_{i+1} + ^{i}\mathbf{v}_i) + \dot{d}_{i+2}\hat{Z}_{i+1} \tag{5}$$

Note that for a prismatic joint, $\dot{\theta}_{i+1} = 0$ in Eq. (4), and for a revolute joint, $\dot{d}_{i+1} = 0$ in Eq. (5).

The Raven IV arm is structured such that the positioning of the surgical tool tip in a 3D workspace only depends on the first three DOFs. The remaining four DOFs dictate the tool tip orientation and, therefore, do not affect the mechanism's kinematic manipulability. As a result, the analytical derivation of the Jacobian takes into account the first three DOFs (i.e., θ_1, θ_2, and d_4) which determine the position of the surgical tool. The irrelevant DOFs, including θ_3, α_4, θ_5, and θ_6, are set to zeros.

According to the velocity propagation method, the angular velocity of the tool's wrist for the left arm is

$$^{3}\mathbf{v}_3 = \begin{bmatrix} c_2 c_\beta s_\alpha \dot{\theta}_1 + s_\beta c_\alpha \dot{\theta}_1 - s_\beta \dot{\theta}_2 \\ s_2 s_\alpha \dot{\theta}_1 \\ c_2 s_\beta s_\alpha \dot{\theta}_1 - c_\beta c_\alpha \dot{\theta}_1 + c_\beta \dot{\theta}_2 \end{bmatrix} \tag{6}$$

and for the right arm is

$$^{3}\mathbf{v}_3 = \begin{bmatrix} -c_2 c_\beta s_\alpha \dot{\theta}_1 - s_\beta c_\alpha \dot{\theta}_1 + s_\beta \dot{\theta}_2 \\ s_2 s_\alpha \dot{\theta}_1 \\ c_2 s_\beta s_\alpha \dot{\theta}_1 - c_\beta c_\alpha \dot{\theta}_1 + c_\beta \dot{\theta}_2 \end{bmatrix} \tag{7}$$

The linear velocities of the tool's wrist are the same for both left and right arms, which are

$$^{3}\mathbf{v}_3 = \begin{bmatrix} 0 \\ 0 \\ \dot{d}_4 \end{bmatrix} \tag{8}$$

Therefore, the analytically derived Jacobian matrix for the left arm is

$$^{3}\mathbf{J} = \begin{bmatrix} c_2 c_\beta s_\alpha + s_\beta c_\alpha & -s_\beta & 0 \\ s_2 s_\alpha & 0 & 0 \\ c_2 s_\beta s_\alpha - c_\beta c_\alpha & c_\beta & 1 \end{bmatrix} \tag{9}$$

and for the right arm is

$$^{3}\mathbf{J} = \begin{bmatrix} -(c_2 c_\beta s_\alpha + s_\beta c_\alpha) & s_\beta & 0 \\ s_2 s_\alpha & 0 & 0 \\ c_2 s_\beta s_\alpha - c_\beta c_\alpha & c_\beta & 1 \end{bmatrix} \tag{10}$$

As shown in Eqs. (9) and (10), the analytical Jacobian matrix has a unit vector corresponding to the prismatic joint along the z-axis of Frame 4. Thus, the mechanism isotropy of a Raven IV arm depends only on the 2×2 top left submatrix of the Jacobian, denoted as $^{3}\mathbf{J}_s$.

2.4 Cost Function. The common workspace is optimized taking into account four goals. The first two are to maximize (1) the sum of the isotropy across the entire common workspace (Σ Iso), and to minimize (2) the isotropy ($\mathrm{Iso}_{\min}$) of the common workspace. We also want to maximize (3) the Area–Circumference ratio (ς) given bounded isotropy values. Finally, we want to maximize (4) the stiffness of the mechanism to reduce the end effector position and orientation errors due to link deformations. In a spherical geometry of the mechanism, the axes of the first three links intersect in a single point, which defines its remote center. The kinematics of the mechanism is independent of the radius of the sphere. As a result, the link lengths of the spherical mechanism are measured by angles, while the radius of a spherical mechanism determines the space around the point where the surgical tool is inserted into the patient's body.

With the above considerations, we define the following cost function of parameters illustrated in Fig. 5 to optimize the mechanical design and configuration of the Raven IV surgical system

$$C = \max_{(\alpha,\beta,\phi_x,\phi_y,\phi_z,b_x,b_y)} \left\{ \frac{\varsigma \cdot \sum \mathrm{Iso} \cdot \mathrm{Iso}_{\min}}{\alpha^3 + \beta^3} \right\} \tag{11}$$

In Eq. (11), $\sum$ Iso denotes the sum of the actual isotropy of the points in the common workspace and $\mathrm{Iso}_{\min}$ denotes the minimum isotropy required in the common workspace. The denominator $\alpha^3 + \beta^3$ describes our goal regarding the maximization of the structure stiffness, which is inversely proportional to the cube of the link lengths.

To summarize, the cost function Eq. (11) maximization computes the following parameters: (1) the link lengths of the first two links α (the angle between the Axis 1 and Axis 2) and β (the angle between Axis 2 and Axis 3); (2) the base orientation of the arms denoted by ϕ_x, ϕ_y, and ϕ_z and measured by the rotations about the axes of the world coordinate frame X_w, Y_w, and Z_w,

Table 2 Parameter ranges and preferred values for the optimization of the Raven IV surgical robotic system

	Range	Optimal value	Resolution
A	[5 deg, 90 deg]	85 deg	20 deg
β	[5 deg, 90 deg]	65 deg	20 deg
ϕ_x	[−20 deg, 20 deg]	20 deg	10 deg
ϕ_y	[−20 deg, 20 deg]	10 deg	10 deg
ϕ_z	[−20 deg, 20 deg]	−20 deg	10 deg
b_x	[50, 200] (mm)	100 (mm)	50 (mm)
b_y	[50, 200] (mm)	50 (mm)	50 (mm)
$\mathrm{Iso}_{\min}$	[0.1, 0.9]	0.5	0.2
Result	$C_{\max} = 526.3338$ for $\mathrm{Iso}_{\min} = 0.5$		

respectively; (3) the port spacing b_x and b_y, which are the horizontal distances between the bases of the Raven IV arms; and (4) the minimum isotropy required in the workspace is denoted by $\mathrm{Iso}_{\min}$.

3 Results

In this section, we use a brute force method to search in the whole parameter space for the parameter values that maximize the value of the cost function. We also study how each individual parameter affects the cost function.

3.1 Overall Optimization. A brute force search in the parameter ranges and with the resolutions listed in Table 2 was conducted to maximize the cost function $C_{\max}$ from expression Eq. (11). The search explored the total of 2.304×10^{10} parameter combinations, each of them representing a specific configuration of the four robotic arms. The configuration that maximizes the cost function is depicted in Fig. 6(*a*). This configuration resulted into the largest circular common workspace shared by the four arms as depicted in Fig. 6(*b*)) with an approximate radius of 150 mm.

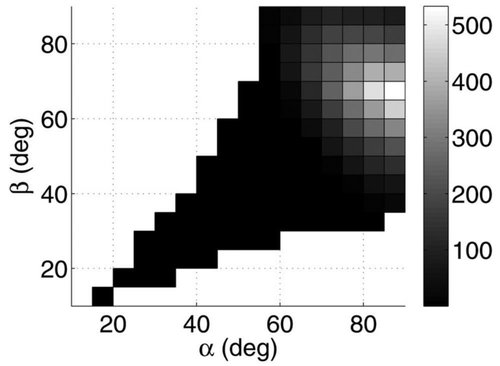

Fig. 7 $C_{\max}$ **as a function of the first two link lengths** α **and** β

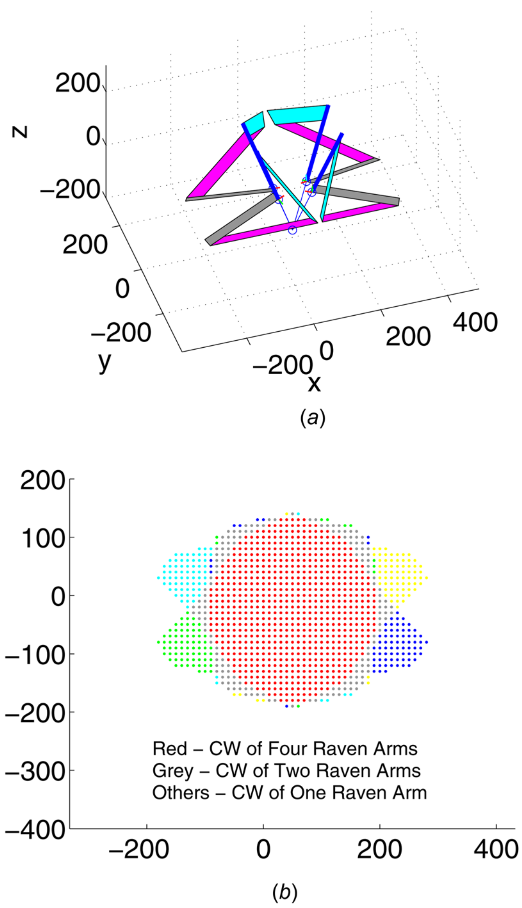

Fig. 6 Optimal configuration of the Raven IV surgical robot four arms following a brute force search (*a*) relative position and orientation of the system bases (*b*) optimized workspace (unit: mm)

Figures 7–10 show trends of $C_{\max}$ with respect to the parameters. According to Fig. 9, the largest $C_{\max}$ value is for maxϕ_x and minϕ_z. For all other optimization parameters, the largest $C_{\max}$ value is in the middle of the parameter ranges. Table 2 shows the parameter ranges, resolutions, and preferred values of our optimization using brute force method, with an optimal $C_{\max}$. To find an even better $C_{\max}$ and its corresponding parameter values, we conduct another brute force search in the neighborhood of the optimal parameter value of α, β, ϕ_y, b_x, b_y, and $\mathrm{Iso}_{\min}$ with refined resolutions ($C_{\max} = 533.01$ when $b_x = 90$ mm).

3.2 Link Length. Given the spherical shape of the mechanism, the lengths of the first two links are expressed as two angles, α and β. These two link lengths are fixed in the design process, whereas other parameters of the Raven robotic arms can be adjusted as part of setting up the system. The size of the workspace of a single Raven arm is maximized when α and β are 90 deg. However, for the rigidity of the mechanism, we generally prefer shorter link lengths. Figure 7 depicts the cost function value $C_{\max}$ for the optimal configuration, while α and β are varied. The figure shows that for $\alpha, \beta \in [0\,\mathrm{deg}, 90\,\mathrm{deg}]$, the unction $C_{\max}$ has the largest value when $\alpha = 85$ deg and $\beta = 65$ deg.

3.3 Isotropy Performance. Limiting the minimal acceptable value of the isotropy $\mathrm{Iso}_{\min}$ has a significant effect on the common workspace optimization result. The Jacobian matrices derived in forward kinematics (see Eqs. (9) and (10)) have three variables, including θ_1 (the shoulder joint angle), θ_2 (the elbow joint angle),

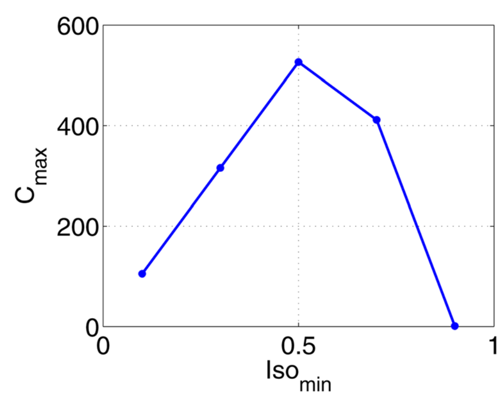

Fig. 8 $C_{\max}$ **varies with** $\mathrm{Iso}_{\min}$

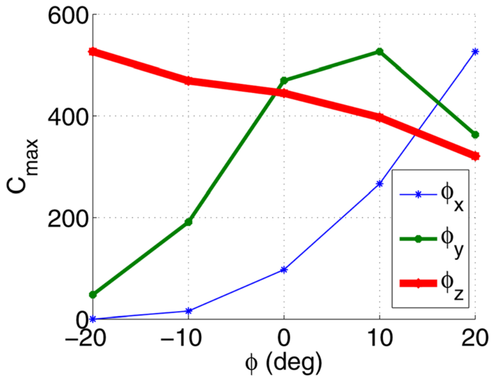

Fig. 9 Effect of base orientation (ϕ_x, ϕ_y, and ϕ_z)

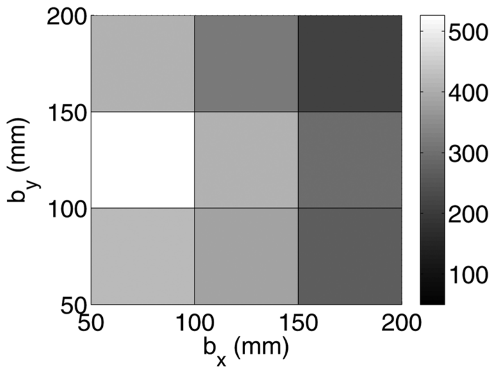

Fig. 10 Performance criteria C_{max} as a function of port spacing along the two orthogonal directions b_x and b_y

and d_4 (the tool shaft displacement). However, as depicted in Fig. 11(*a*), the plot of the isotropy as a function of θ_1 and θ_2 indicates that the isotropy of the Raven robotic arm mechanism varies only with θ_2. In Fig. 11, we choose the different $\mathrm{Iso}_{\min}$ in the common workspace to show that the θ_2 value range shrinks as $\mathrm{Iso}_{\min}$ increases, regardless of arm configuration and link length.

We further find that $\mathrm{Iso}_{\min}$ affects the shape of the common workspace, the optimal link lengths, and the maximum of the cost function. Figure 12 depicts the area–circumference ratio ς as a function of link lengths α and β for different $\mathrm{Iso}_{\min}$. Figure 8 further shows that $C_{\max}$ varies with $\mathrm{Iso}_{\min}$ and is maximal when $\mathrm{Iso}_{\min} = 0.5$.

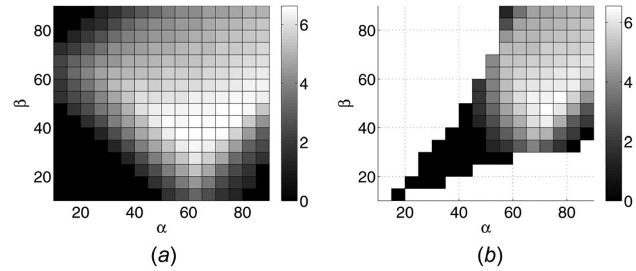

Fig. 12 $\mathrm{Iso}_{\min}$ affects the optimized shape of the common workspace depicted by the area-circumference ratio ς as a function of link lengths: (*a*) when $\mathrm{Iso}_{\min} = 0$ then $\varsigma_{\max} = 6.64$, and the optimal link lengths are $\alpha = 80$ deg and $\beta = 40$ deg and (*b*) when $\mathrm{Iso}_{\min} = 0.5$ then $\varsigma_{\max} = 6.55$, and the optimal link lengths are $\alpha = 70$ deg, $\beta = 35$ deg

3.4 Robot Base Orientation. The base orientation of each Raven arm is determined by three rotation angles in the world coordinate system. The rotation angles about the X_w, Y_w, and Z_w axes are denoted by ϕ_x, ϕ_y, and ϕ_z, respectively. A mirror image axial symmetry is assumed for the rotations with respect to all the axes and the following text refers to the top right Raven arm (first quadrant) in Fig. 13(*a*).

Figure 9 shows $C_{\max}$ as a function of the base orientation in each individual axis, $\phi_x, \phi_y, \phi_z \in [-20\,\mathrm{deg}, 20\,\mathrm{deg}]$. When varying one of the angles ϕ_x, ϕ_y, or ϕ_z, the rest of them are set to zeros. In Fig. 9, $C_{\max}$ monotonously increases with ϕ_x, monotonously decreases with ϕ_z, and it reaches its maximum for $\phi_y = 10\,\mathrm{deg}$. The diagram shows that $C_{\max}$ is most sensitive to the change in the base rotation about the x-axis and least sensitive to the change in the base rotation about the z-axis.

In Fig. 14, we plot $C_{\max}$ as a function of various combinations of base orientations in three perpendicular planes. Figure 13 shows the top, front, and side views of the four Raven IV arms for the optimal base orientation, i.e., $\phi_x = 20\,\mathrm{deg}$, $\phi_y = 10\,\mathrm{deg}$, and $\phi_z = -20\,\mathrm{deg}$.

3.5 Port Spacing. Figure 10 depicts $C_{\max}$ as a function of port spacing and shows that it monotonically decreases as the distance between the ports along the x-axis increases, while it reaches its maximum when the distance between the ports along the y-axis is 100 mm. As a result, the expected benefit is maximized by separating the port locations 50 mm along the x-axis and 100 mm along the y-axis. This result coincides with empirical data of port placement in minimally invasive surgical applications.

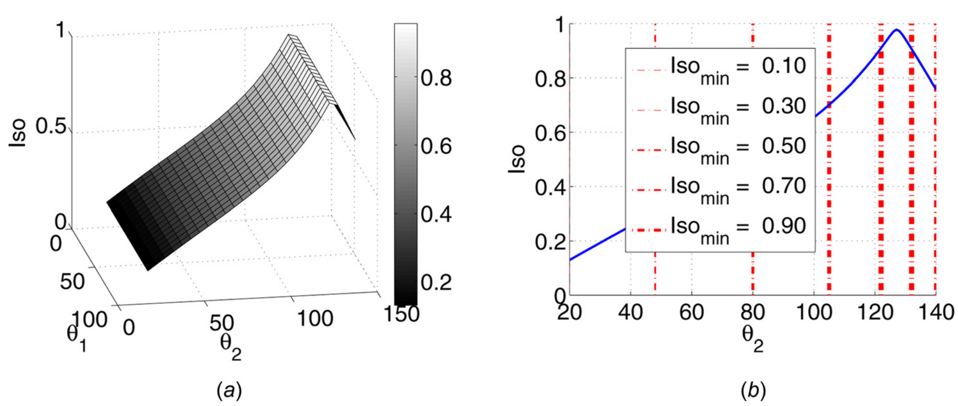

Fig. 11 The representative plot of the mechanism isotropy as a function of θ_1 and θ_2 for the first two link lengths $\alpha = 55$ deg and $\beta = 40$ deg: (*a*) the mechanism isotropy of the Raven arm as a function of θ_1 and θ_2, showing that the isotropy does not depend on θ_1 and (*b*) the mechanism isotropy of the Raven arm as a function of θ_2, showing that the minimal required workspace isotropy $Iso_{\min}$ limits the range for θ_2

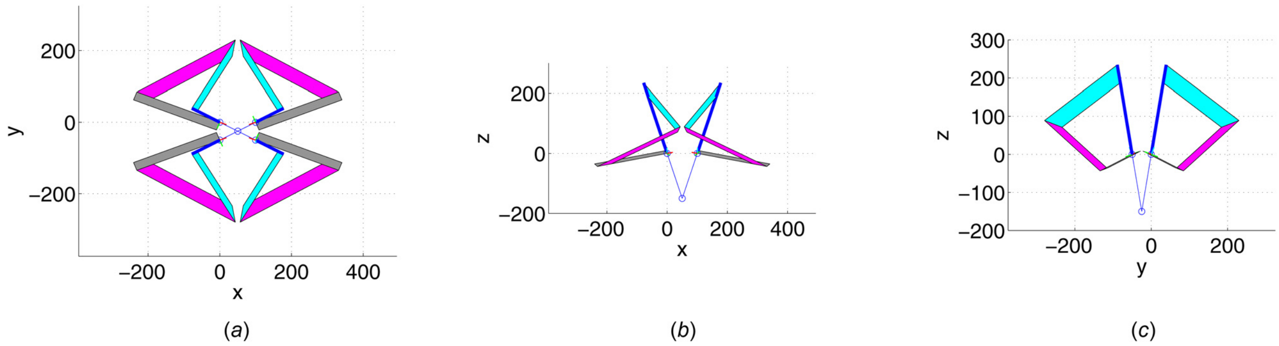

Fig. 13 The top, front and side views of the four Raven IV arms (unit: mm): (*a*) top view, (*b*) front view, and (*c*) side view

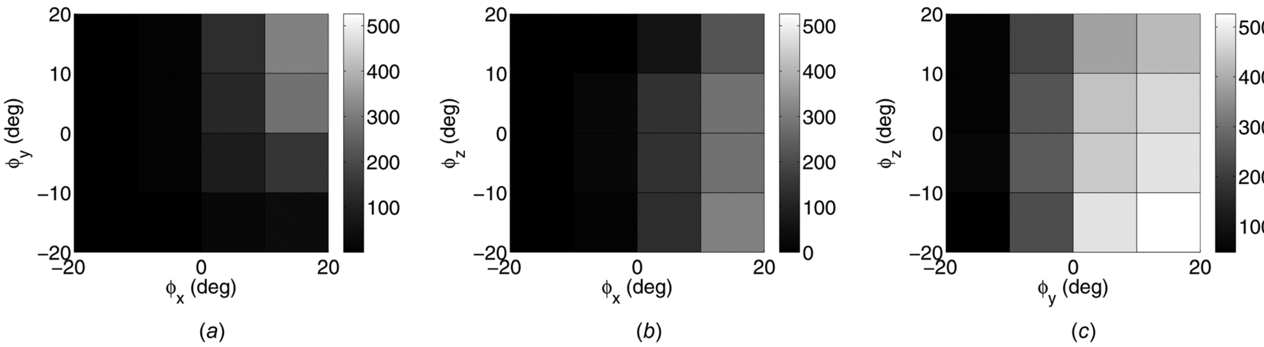

Fig. 14 C_{max} is plotted as a function of various base orientations (ϕ_x, ϕ_y, and ϕ_z)

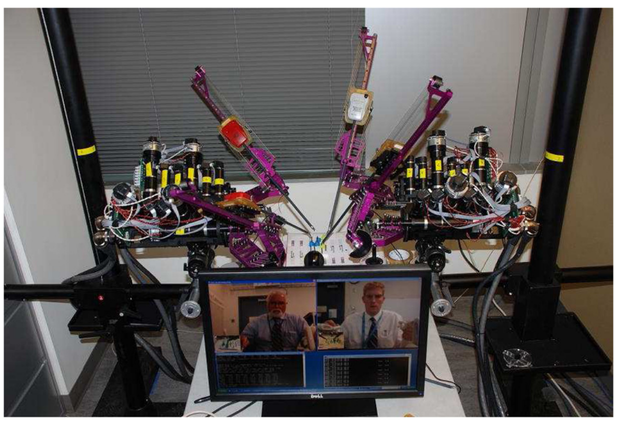

Fig. 15 Raven IV surgical robotic system—preliminary teleoperation experiment depicting two surgeons located at the University of Washington campus in Seattle WA teleoperated the four Raven arm system located in the University of California, Santa Cruz, CA using a commercial Internet connection

4 Conclusions and Discussion

Providing a couple of surgeons the level of access, manipulability, dexterity of the surgical site, as well as the visual views of it via robotic technology requires at least four robotic arms and two stereo cameras rendering the surgical site. The core of this research was to optimize the design of four surgical robotic arms to maximize the shared workspace while both maximizing the manipulatable factors and stiffness, and minimizing their footprint. Given the generic nature of the surgical robotic system, its design did not target any specific anatomical structures or surgical procedures.

The design parameters of the system can be divided into two groups (1) design parameters that are fixed following the fabrication of the robotic arms, i.e., angular link lengths, and (2) design parameters that are changeable at any point during the operation of the system, i.e., positions and orientations of the individual robotic arms, as well as the relationship between them, i.e., spacing between the bases and the relative orientation to each other and the surgical site.

The cost function for optimizing the design accounts for geometry kinematics and stiffness parameters. The effect of each parameter was studied individually followed by the brute force search across the range of all the parameters. The effects of the individual parameters on the isotropy, link lengths, and base orientation are as follows:

Isotropy: The analytical derivation of the system shows that the mechanism isotropy performance of a Raven arm depends on a 2×2 submatrix of the 3×3 Jacobian matrix for the end effector positioning (i.e., θ_1, θ_2 and d_4) once the Jacobian matrix is expressed in the coordinate of the tool's shaft. Given the spherical shape of the mechanism, the isotropy is a function only of the elbow joint. The maximal and minimal values are functions of the two link lengths. Bounding the mechanism isotropy ensures high performance of the entire system. An increase of the minimum acceptable value of the isotropy leads to a smaller common workspace. However, the overall performance criterion is maximized once the minimal isotropy is set to 0.5.

Link Lengths: The first two links of the mechanism were optimized. Given the spherical geometry of the mechanism, the link lengths are expressed as angles. The kinematics of the mechanism is independent of the sphere's radius. The radius is set to provide sufficient space to encapsulate the MIS port. Setting the angles of the first two links to be 90 deg each allows to position the end effector at the tip of the tool inserted along the radius anywhere in the sphere. However, there are two major disadvantages in setting the link angular length to this value. First, the longer the link, the more flexible is the mechanism. Second, if the link angular length is longer, there is a higher chance of collision between the surgical robotic arms and the body of the patient. Optimizing the mechanism for link angular length shows that as the link length increases, the performance criterion improves; however, the best performance is accomplished when the link lengths are set to $\alpha = 85$ deg and $\beta = 65$ deg. Setting the minimal isotropy to a value of 0.5 eliminates some combinations of link length angles.

Base Orientation: The base orientation is dictated by three angles. Among the three axes, the cost function is highly sensitive to changes along the two angles that define the plane of the base and less sensitive to changes along the axis that is perpendicular to the base. The optimal solution of the base configuration results in a configuration forming an X shape in the coronal plane, a convex shape in the axial plane, and a concave shape in the sagittal plane. It is interesting to note that the configuration of the bases is similar to the orientation of the palms of two surgeons interacting with the surgical site while standing at each side of the operating room table.

Port Spacing: Creating the shared workspace with a circular geometry is accomplished by spacing the bases 50 mm along the superior/inferior axis and 100 mm along the left/right axis. Analyzing the clinical port placement in MIS indicates similar distances.

The brute force optimization followed the detailed study of the individual parameters to identify the combination of parameters that maximizes the cost function. The combination defines the structural geometry of the mechanism, and the relative positions and originations of its four surgical robotic arms with respect to each other in order to maximize the circular shaped common workspace of the four arms. The introduction of multiple robotic arms into the surgical field enables several operational modes in which each pair of arms can be under full human control or in a semi-autonomous mode (supervisory control). Although the primary focus of the current study is surgical robotic system design, the proposed design methodology can be generalized and applied to a wider spectrum of robotic arms aimed at sharing a common workspace with kinematic constrains.

Following its optimization, detailed design, fabrication, and integration, the system was initially tested using a collaborative mode. Two surgeons located at the University of Washington campus in Seattle, WA teleoperated the system collaboratively each controlling a pair of the Raven arms while completing fundamental laparoscopic skill (FLS) tasks using a commercial Internet connection (see Fig. 15). The preliminary results indicate the feasibility of two surgeons to either interact with each other while performing collaborative effort or conduct two parallel tasks toward completion of their joint work.

Appendix

Here, we present the derivation of the forward and inverse kinematics of the Raven surgical robotic arms. In this section, $\sin\theta_i$ is denoted as s_i, $\cos\theta_i$ as c_i, $\sin\alpha_i$ as $s\alpha_i$, and $\cos\alpha_i$ as $c\alpha_i$.

The direct kinematics can be derived from Table 1

$$ {}^0_6T = {}^0_1T \cdot {}^1_2T \cdot {}^2_3T \cdot {}^3_4T \cdot {}^4_5T \cdot {}^5_6T = \begin{bmatrix} r_{11} & r_{12} & r_{13} & P_x \\ r_{21} & r_{22} & r_{23} & P_y \\ r_{31} & r_{32} & r_{33} & P_z \\ 0 & 0 & 0 & 1 \end{bmatrix} \tag{A1} $$

Given the position and orientation of the end effector of a Raven IV arm, each arm has seven DOFs. However, the two jaws of the tool effector and its wrist were reduced to a single DOF. With this approach, the system as a whole was reduced mathematically to a six DOF system with a close form inverse kinematics solution. The physical joint limits defined by Table 1 were added to the analytical description to ensure the ability of the arm to reach a specific point in space.

Equation (A1) describes the homogeneous transformation of the Raven IV arm kinematics.

Hence, ${}^6_0T$ can be determined as the inverse of ${}^0_6T$ such that

$$ {}^6_0T = \begin{bmatrix} r'_{11} & r'_{12} & r'_{13} & P_{\text{xinv}} \\ r'_{21} & r'_{22} & r'_{23} & P_{\text{yinv}} \\ r'_{31} & r'_{32} & r'_{33} & P_{\text{zinv}} \\ 0 & 0 & 0 & 1 \end{bmatrix} \tag{A2} $$

where for the left robotic arm

$$ \begin{aligned} P_{\text{xinv}} &= (-d_4c_5 + a_5)c_6 \\ P_{\text{yinv}} &= s_5d_4 \\ P_{\text{zinv}} &= (-d_4c_5 + a_5)s_6 \end{aligned} \tag{A3} $$

and for the right robotic arm

$$ \begin{aligned} P_{\text{xinv}} &= (d_4c_5 - a_5)c_6 \\ P_{\text{yinv}} &= s_5d_4 \\ P_{\text{zinv}} &= (-d_4c_5 + a_5)s_6 \end{aligned} \tag{A4} $$

Let us define P_{inv} as

$$ \begin{aligned} P^2_{\text{inv}} &= (P^2_{\text{xinv}} + P^2_{\text{yinv}} + P^2_{\text{zinv}}) \\ &= (d_4c_5 - a_5)^2c_6^2 + s_5^2d_4^2 + (-d_4c_5 + a_5)^2s_6^2 \\ &= (a_5 - d_4c_5)^2 + s_5^2d_4^2 \\ &= a_5^2 - 2a_5d_4c_5 + d_4^2c_5^2 + s_5^2d_4^2 \\ &= a_5^2 - 2a_5d_4c_5 + d_4^2 \end{aligned} \tag{A5} $$

which gives

$$ c_5^2 = \left(\frac{a_5^2 + d_4^2 - P^2_{\text{inv}}}{2a_5d_4}\right)^2 \tag{A6} $$

Note that both Eqs. (A3) and (A4) lead to

$$ c_5^2 = 1 - s_5^2 = 1 - (P_{\text{yinv}}/d_4)^2 \tag{A7} $$

Hence

$$ 1 - \left(\frac{P_{\text{yinv}}}{d_4}\right)^2 = \left(\frac{a_5^2 + d_4^2 - P^2_{\text{inv}}}{2a_5d_4}\right)^2 \tag{A8} $$

Equation (A8) satisfies both the left and the right robotic arms and, therefore, leads to four possible solutions to d_4

$$ d_{41} = \sqrt{a_5^2 + P^2_{\text{inv}} + 2a_5\sqrt{(P^2_{\text{inv}} - P^2_{\text{yinv}})}} \tag{A9} $$

$$ d_{42} = -\sqrt{a_5^2 + P^2_{\text{inv}} + 2a_5\sqrt{(P^2_{\text{inv}} - P^2_{\text{yinv}})}} \tag{A10} $$

$$ d_{43} = \sqrt{a_5^2 + P^2_{\text{inv}} - 2a_5\sqrt{(P^2_{\text{inv}} - P^2_{\text{yinv}})}} \tag{A11} $$

$$ d_{44} = -\sqrt{a_5^2 + P^2_{\text{inv}} - 2a_5\sqrt{(P^2_{\text{inv}} - P^2_{\text{yinv}})}} \tag{A12} $$

of which only Eq. (A12) is acceptable for both the left and right arms given the constraints in Table 1.

The angle θ_6 can be resolved as

$$ s_6 = P_{\text{zinv}}/(-d_4c_5 + a_5) \tag{A13} $$

for the left arm

$$c_6 = P_{\text{xinv}}/(-d_4 c_5 + a_5) \tag{A14}$$

and for the right arm

$$c_6 = -P_{\text{xinv}}/(-d_4 c_5 + a_5) \tag{A15}$$

$$\theta_6 = \text{Atan2}(s_6, c_6) \tag{A16}$$

The angle θ_5 can be resolved as

$$s_5 = P_{\text{yinv}}/d_4 \tag{A17}$$

$$c_5 = \sqrt{1 - s_5^2} \tag{A18}$$

$$\theta_5 = \text{Atan2}(s_5, c_5) \tag{A19}$$

Given the solution of d_4, θ_5, and θ_6, we can compute

$$\begin{aligned} {}^0_3T &= {}^0_1T \cdot {}^1_2T \cdot {}^2_3T = {}^0_6T \cdot [{}^3_4T \cdot {}^4_5T \cdot {}^5_6T]^{-1} \\ &= \begin{bmatrix} a_{11} & a_{12} & a_{13} & a_x \\ a_{21} & a_{22} & a_{23} & a_y \\ a_{31} & a_{32} & a_{33} & a_z \\ 0 & 0 & 0 & 1 \end{bmatrix} \end{aligned} \tag{A20}$$

where

$$a_{32} = s_2 s_\alpha c_3 + (c_2 s_\alpha c_\beta + c_\alpha s_\beta) s_3 \tag{A21}$$

$$a_{33} = c_2 s_\alpha s_\beta - c_\alpha c_\beta \tag{A22}$$

The angle θ_2 can be resolved as

$$c_2 = \frac{c_\alpha c_\beta + a_{33}}{s_\alpha s_\beta} \tag{A23}$$

$$s_2 = \sqrt{1 - c_2^2} \tag{A24}$$

$$\theta_2 = \text{Atan2}(s_2, c_2) \tag{A25}$$

Let us define $a = s_2 s_\alpha$ and $b = c_2 s_\alpha c_\beta + c_\alpha s_\beta$. Thus, Eq. (A21) becomes

$$a_{32} = a c_3 + b s_3 \tag{A26}$$

and a, b, and a_{32} are known. Eq. (A26) can be solved with the tangent-of-the-half-angle substitutions (see Sec. 4.5 of Ref. [18])

$$\theta_3 = 2\text{Atan}\left(\frac{b \pm \sqrt{a^2 + b^2 - a_{32}^2}}{a + a_{32}}\right) \tag{A27}$$

Equation (A26) can also be solved as (see C.10 of Ref. [18]):

$$\theta_3 = \text{Atan2}(b, a) \pm \text{Atan2}(\sqrt{a^2 + b^2 - a_{32}^2}, a_{32}) \tag{A28}$$

Note that solutions only exist when $a^2 + b^2 - a_{32}^2 \geq 0$. Additionally, Eq. (A27) requires $a + a_{32} \neq 0$ and Eq. (A28) requires $a_{32} \neq 0$ and $a \neq 0$.

An algorithm to check a_{13} (Eqs. (A29) and (A30)) in Eq. (A20)) can be used to choose between the two possible solutions of θ_3.

For the left arm,

$$a_{13} = -s_2 s_\alpha s_3 + c_2 s_\alpha c_3 c_\beta + c_\alpha c_3 s_\beta \tag{A29}$$

For the right arm

$$a_{13} = s_2 s_\alpha s_3 - c_2 s_\alpha c_3 c_\beta - c_\alpha c_3 s_\beta \tag{A30}$$

Given the solution for θ_2 and θ_3, θ_1 can be determined by

$$\begin{aligned} {}^0_1T &== {}^0_6T \cdot [{}^3_4T \cdot {}^4_5T \cdot {}^5_6T]^{-1} [{}^1_2T \cdot {}^2_3T]^{-1} \\ &= \begin{bmatrix} b_{11} & b_{12} & b_{13} & b_x \\ b_{21} & b_{22} & b_{23} & b_y \\ b_{31} & b_{32} & b_{33} & b_z \\ 0 & 0 & 0 & 1 \end{bmatrix} \end{aligned} \tag{A31}$$

with $s_1 = b_{11}$, $c_1 = b_{21}$ for the left robot, $s_1 = b_{11}$, $c_1 = b_{21}$ for the right robot and

$$\theta_1 = \text{Atan2}(s_1, c_1) \tag{A32}$$

References

[1] Selha, S., Dupont, P., Howe, R., and Torchiana, D., 2001, "Dexterity Optimization by Port Placement in Robot-Assisted Minimally Invasive Surgery," Proc. SPIE, **4570**, pp. 97–104.

[2] Cannon, J., Stoll, J., Selha, S., Dupont, P., Howe, R., and Torchiana, D., 2003, "Port Placement Planning in Robot-Assisted Coronary Artery Bypass," IEEE Trans. Rob. Autom., **19**(5), pp. 912–917.

[3] Trejos, A., and Patel, R., 2005, "Port Placement for Endoscopic Cardiac Surgery Based on Robot Dexterity Optimization," IEEE International Conference on Robotics & Automation (ROBOT), Barcelona, Spain, Apr. 18–22, pp. 912–917.

[4] Bauernschmitt, R., Feuerstein, M., Traub, J., Schirmbeck, E., Klinker, G., and Lange, R., 2007, "Optimal Port Placement and Enhanced Guidance in Robotically Assisted Cardiac Surgery," Surg. Endoscopy, **21**(4), pp. 684–687.

[5] Li, J., Wang, S., Wang, X., and He, C., 2010, "Optimization of a Novel Mechanism for a Minimally Invasive Surgery Robot," Int. J. Med. Rob. Comput. Assisted Surg., **6**(1), pp. 83–90.

[6] Lum, M., Friedman, D. C. W., Sankaranarayanan, G., King, H. K. F., II, Leuschke, R., Hannaford, B., Rosen, J., and Sinanan, M. N., 2009. "The Raven—A Multidisciplinary Approach to Developing a Telesurgery System," IJRR, **28**(9), pp. 1183–1197.

[7] Lum, M., Rosen, J., Lendvay, T. S., Sinanan, M. N., and Hannaford, B., 2009, "Effect of Time Delay on Telesurgical Performance," IEEE International Conference on Robotics and Automation (ICRA '09), Kobe, Japan, May 12–17, pp. 4246–4252.

[8] Lum, M. J., Rosen, J., King, H., Friedman, D., Lendvay, T., Wright, A. S., Sinanan, M. N., and Hannaford, B., 2009, "Teleoperation in Surgical Robotics—Network Latency Effects on Surgical Performance," Annual International Conference of the IEEE Engineering in Medicine and Biology Society (EMBS 2010), Minneapolis, MN, Sept. 3–6, pp. 6860–6863.

[9] Lum, M. J., Rosen, J., Lendvay, T., Wright, A. S., Sinanan, M. N., and Hannaford, B., 2008, "TeleRobotic Fundamentals of Laparoscopic Surgery (FLS): Effects of Time Delay—Pilot Study," 30th Annual Conference of the IEEE Engineering in Medicine and Biology Society (IEMBS), Vancouver, Canada, Aug. 20–25, pp. 5597–5600.

[10] Brett, H., Doarn, C., Rosen, J., Hannaford, B., and Broderick, T. J., 2008, "Evaluation of Unmanned Airborne Vehicles and Mobile Robotic Telesurgery in an Extreme Environment," Telemedicine J. E-Health, **14**(6), pp. 534–544.

[11] Lum, M., Friedman, D., Sankaranarayanan, G., King, H., Wright, A., Sinanan, M., Lendvay, T., Rosen, J., and Hannaford, B., 2008, "Objective Assessment of Telesurgical Robot Systems: Telerobotic FLS," Medicine Meets Virtual Reality (MMVR 16), Long Beach, CA, Jan. 30–Feb. 1, pp. 263–265.

[12] Sankaranarayanan, G., Hannaford, B., King, H., Ko, S., Lum, M., Friedman, D., Rosen, J., and Hannaford, B., 2007, "Portable Surgery Master Station for Mobile Robotic Surgery," 1st International Conference on Robot Communication and Coordination (RoboComm '07), Athens, Greece, Oct. 15–17, p. 28.

[13] Lum, M., Friedman, D., King, H., Donlin, R., Sankaranarayanan, G., Broderick, T., Sinanan, M., Rosen, J., and Hannaford, B., 2007, "Teleoperation of a Surgical Robot Via Airborne Wireless Radio and Transatlantic Internet Links," *Field and Service Robots* (Springer Tracts in Advanced Robotics), Vol. 42, Springer, Berlin, pp. 305–314.

[14] Lum, M., Rosen, J., King, H., Friedman, D., Donlin, G., Sankaranarayanan, G., Harnett, B., Huffman, L., Doarn, C., Broderick, T., and Hannaford, B., 2007, "Telesurgery Via Unmanned Aerial Vehicle (UAV) With a Field Deployable

Surgical Robot," Medicine Meets Virtual Reality (MMVR 15), Long Beach, CA, Feb. 6–9, pp. 313–315.
[15] Lum, M., Rosen, J., Sinanan, M., and Hannaford, B., 2006, "Optimization of Spherical Mechanism for a Minimally Invasive Surgical Robot: Theoretical and Experimental Approaches," IEEE Trans. Biomed. Eng., **53**(7), pp. 1440–1445.
[16] Rosen, J., Lum, M., Sinanan, M., and Hannaford, B., 2011, "Raven: Developing a Surgical Robot From a Concept to a Transatlantic Teleoperation Experiment," *Surgical Robotics, Systems, Applications, and Visions*, 1st ed., R. M. Satava, ed., Springer, New York.
[17] Lum, M., Rosen, J., Sinanan, M., and Hanaford, B., 2004, "Kinematic Optimization of a Spherical Mechanism for a Minimally Invasive Surgical Robot," IEEE International Conference on Robotics and Automation (ICRA 2004), New Orleans, LA, Apr. 26–May 1, pp. 829–834.
[18] Craig, J., 2003, *Introduction to Robotics: Mechanics and Control*, 3rd ed., Prentice Hall, Upper Saddle River, NJ, Chap. 1.